Available online at www.sciencedirect.com

SciVerse ScienceDirect

Ceramics International 39 (2013) 4205–4212

CERAMICS INTERNATIONAL

www.elsevier.com/locate/ceramint

Linking microstructure evolution and impedance behaviors in spark plasma sintered Si_3N_4/TiC and Si_3N_4/TiN ceramic nanocomposites

Bernard Haochih Liu[a,b,*], Po-Jui Su[a], Ching-Huan Lee[a], Jow-Lay Huang[a]

[a]*Department of Materials Science and Engineering, National Cheng Kung University, Taiwan ROC*
[b]*Promotion Center for Global Materials Research, National Cheng Kung University, Taiwan ROC*

Received 25 October 2012; received in revised form 2 November 2012; accepted 2 November 2012
Available online 8 November 2012

Abstract

We proposed a novel approach to investigate the three-dimensional microstructures and sintering behaviors of Si_3N_4-based ceramic nanocomposites by electrochemical impedance spectroscopy. Si_3N_4/TiC and Si_3N_4/TiN with various weight percentages of conductive phases were prepared by spark plasma sintering (SPS) at different temperatures and dwell times. The incorporation of TiC and TiN into β-Si_3N_4 provides pulse current paths inside the ceramics due to their higher conductivity. These paths enable the localized Joule heating and mass transport, facilitating the densification and grain growth of ceramic compact. The electrochemical study of such nanocomposites has revealed three-dimensional information of the evolution of their microstructures, and the capacitive and resistive characteristics of the nanocomposites reflect the densification, grain growth, and element distribution in the compact. The impedance model presented in this work suggests isolated distribution of TiN in Si_3N_4 while Si_3N_4/TiC of the same amount of additives at the same sintering conditions formed conductive network. This impedance analysis further explained the differences in densification mechanism of SPS in Si_3N_4/TiN and Si_3N_4/TiC.

Keywords: B. Microstructure; C. Impedance; Silicon nitride; Spark plasma sintering

1. Introduction

Spark plasma sintering (SPS), a field-activated process in which a pulsed electric current is applied to densify ceramic powders, has attracted significant research interest due to its high efficiency and low energy consumption. In addition to Joule heating and pressure-assisted sintering processes, SPS applies voltage to induce a direct current through the ceramic compact, and thus the sintering mechanism of SPS can be affected by the electric fields and the electrical characteristics of the powder compact. Due to the improved properties of SPS materials reported in many prior studies [1–7], this process is now being more widely applied. Nonetheless, many of the fundamental phenomena related to SPS are still not well-understood. For instance, the existence of plasma remains controversial, and to date the weight of the conflicting evidence is against the formation of plasma on the powder surface [8–13]. Moreover, the distinctive low-voltage, high-intensity pulsed current in the SPS process has raised a number of interesting questions, such as how pulsed current affects sintering. Researchers have investigated the effects of the pulsed current in the SPS process, and have demonstrated that both the pulsing patterns and frequencies have little relation to the evolution of the related microstructures [10,14–18].

On the other hand, the induced current is believed to influence the temperature distribution in the powder compact. For example, Matsugi et al. measured and calculated the temperature distribution in SPS punch-die-compact systems, and concluded that the voltage and current distribution in conductive (Ti) and insulating (Al_2O_3) compacts were similar, while the temperature distribution changed with the resistivity of the compact powders [19]. Finite element analysis has also been applied

*Corresponding author at: Department of Materials Science and Engineering, National Cheng Kung University, 1 University Rd, Tainan 701, Taiwan ROC. Tel.: +886 6 2757575x62926; fax: +886 6 234 6290.
E-mail addresses: hcliu@mail.ncku.edu.tw, hcliu@alumni.stanford.edu (B.H. Liu).

0272-8842/$ - see front matter © 2012 Elsevier Ltd and Techna Group S.r.l. All rights reserved.
http://dx.doi.org/10.1016/j.ceramint.2012.11.002

to model the temperature gradient inside the die, and the results suggest that the temperature differences depend on the heating rate and thermal conductivity of the powders [20–23].

Recently, SPS has been used in the sintering of heterogeneous powder systems. For instance, Huang et al. fabricated ceramic composites consisting of alumina and carbon nanotubes (CNT) and investigated the high-current-induced damage that occurred to carbon nanotubes in alumina during the SPS process [24], while Belmonte et al. reported the production of tailored microstructures in novel Si_3N_4-based ceramics, such as functionally graded materials and Si_3N_4/CNT composites [25]. Because silicon nitride and its composites are important structural ceramics for cutting tools and engine parts due to their excellent wear resistance, high strength–weight ratio, and superior thermal stability, using the SPS techniques to further improve the properties of Si_3N_4-based composites has became a promising research avenue. Nonetheless, the sintering mechanisms of Si_3N_4-based ceramics during SPS still need to be better understood in order to obtain better control the microstructures of novel ceramic systems.

To address this gap in the literature, this paper thus undertakes electrochemical impedance analyses of ceramic nanocomposite materials. As SPS techniques exhibit unique electric-field-activated phenomena that facilitate the transportation of matter, the measurement of impedance in Si_3N_4/TiC and Si_3N_4/TiN nanocomposites is a superior way to investigate such sintering mechanisms. Although electron microscopy can provide information on microstructures and chemical composition, the investigations are restricted to sectioned specimen area (i.e., two dimensional); impedance spectroscopy, depending on the configuration of electrodes, is capable of probing a volume mass of material to construct three-dimensional analytic results. Unlike prior research that measure resistance of ceramics to access the information on conductive phases [26], impedance measurements reveal important capacitive and resistive characteristics of grains, grain boundary (interfaces), and the conductive phases. Furthermore, using equivalent circuit model to analyze impedance spectra gives crucial information on the microstructures and phase distributions. The relationships among microstructures, process parameters, and impedance responses can provide insights in the densification of Si_3N_4-based nanocomposites, and it is our goal to understand the connections between the SPS process and material properties via electrochemical impedance analysis.

2. Materials and methods

The starting powders were nanosized Si_3N_4 with sintering additives of 6 wt% Y_2O_3 and 8 wt% Al_2O_3 (SM131, Fraunhofer-Institut fur Karamische Technologien and Sinterwerkstoffe, Dresden, Germany). The average size of the particles was 70 nm, as determined by the Rietveld method, and the content of β-phase and α-phase Si_3N_4 was 90 wt% and 10 wt%, respectively. The titanium carbide powders (Hefei Kiln Nanometer Technology Development, Hefei, China) were also nanosized and had an average particle size of 60 nm. The chemical content of the titanium carbide powders was measured using a carbon sulfur determinator and nitrogen/oxygen analyzer (CS-244 and TC-436, Leco Corp., U.S.A.), and the chemical composition of TiC powder was $TiC_{0.72}O_{0.17}N_{0.11}$, with 99% purity.

The conductive TiC nanopowders were mixed with Si_3N_4 nanopowders in ethanol with a 15-min ultrasonic dispersion step, followed by 6-h planetary milling at a rotation speed of 300 rpm. After milling, the slurry was dried by a rotary evaporator, screened via a 200-mesh sieve after 200-MPa cold isostatic pressing and crushing. For the experiment, the conductive TiC nanopowders were added to the Si_3N_4 nanopowders at the weight percentages of 0 wt%, 5 wt%, 10 wt%, and 20 wt%; these samples are labeled Si_3N_4/0TiC, Si_3N_4/5TiC, Si_3N_4/10TiC, and Si_3N_4/20TiC, respectively.

For comparison purposes, titanium nitride (TiN) nanopowders (Hefei Kiln Nanometer Technology Development, Hefei, China) were also added to Si_3N_4 nanopowders to make Si_3N_4/TiN nanocomposites. The average particle size was ~30 nm, and the compositions were also chosen as 5 wt%, 10 wt%, 20 wt%, and 30 wt% of TiN.

The ceramic test samples were prepared by a spark plasma sintering technique, and the system used was Dr. Sinter 1050 (Sumitomo Coal Mining, Kawasaki, Japan). A mixture of 3 g Si_3N_4/TiC powders was placed into a graphite mold (inner diameter = 20 mm, outer diameter = 50 mm, and height = 50 mm) that was covered in carbon insulation. The gap between the punch and mold was shimmed with graphite sheets. The sintering chamber was first vacuumed to 10 Pa and then heated to the target sintering conditions with uniaxial pressure of 30 MPa. The temperature was brought to 600 °C within 3 min, and was ramped to the final densification temperature at a fixed rate of 200 °C/min; after a scheduled dwell time, the power to the SPS system was shut off. The cooling rate after the power shut off was 200 °C/min when the temperature was above 1000 °C.

During SPS, the voltage was maintained in the range of 2–4 V, and the current was 1800–2200 A. The electric power was applied in a 12:2 (pulse/vacancy) pattern, with 3 ms on-time and 1 ms off-time for each pulse.

Note the temperature referred to here is the temperature measured at the die surface, and the actual sample temperature could be 70–180 °C higher [27–29]. After the samples were sintered at the densification temperature, their as-sintered shape was a disk with a diameter of about 19 mm and a thickness of about 3 mm.

The characterizations of the microstructure were carried out by both field emission scanning electron microscopy (FESEM, XL-40FEG, Philips, The Netherlands) and transmission electron microscopy (FEG-TEM, Tecnai G2 F20, Philips, The Netherlands). The as-sintered ceramic samples were cut, ground, and polished using the standard diamond

polishing technique. To reveal the grain boundary of the Si_3N_4 and TiC, reactive ion etching (OMNI-RIE, Duratek Inc., Taiwan) was applied to the specimens after polishing.

The electrochemical characterization was conducted using an electrochemistry impedance spectroscopy (EIS) system (Gamry G300 potentiostat, Gamry Instruments, U.S.A.) with a self-designed sample fixture (Fig. 1) to ensure a uniform parallel electric field during the measurements. Note the measurement is done through the inner plate (shown in the bottom electrode in Fig. 1) under a larger parallel electric field to prevent irregular stray fields near the edge of electrodes. Ceramic samples were ground and polished to a fixed thickness of 2 mm. Silver paste was then applied to both polished sides, baked for several hours at 100 °C and cooled to room temperature before applying the parallel-plated sample fixture. The EIS measurements were carried out in potential static mode, with the AC frequency ranging from 300 kHz to 100 mHz, a direct (biased) voltage of zero, and alternating voltage V_{ac} from 1 mV to 100 mV. A self-designed Faraday cage was also used during measurements to minimize the interference of stray electromagnetic signals from the environment.

3. Results and discussion

3.1. Sintering conditions and impedance responses

Fig. 2 shows the impedance responses of the Si_3N_4/10%TiC samples in various sintering condition, while; the apparent density, average grain size, and the equivalent circuit model for the impedance responses are summarized in Table 1. The Nyquist plot indicates the real and imaginary parts of impedance Z, where Z is the frequency domain ratio of the voltage to the current in a material being tested under an alternating current (AC) circuit. The apparent density of the ceramic compact increased as the sintering temperature rose from 1340 °C to 1650 °C, while the average grain size also increased due to grain growth. However, since the addition of TiC or TiN nanopowder suppresses the grain growth of Si_3N_4, the average grain size in the SPS samples was still in the nanoscale [26,30]. In the analysis of the impedance responses, we propose an equivalent circuit model consisting of multiple sets of "resistor-capacitor-in-parallel" component units linked in series. This model simulates the grains (including grain boundaries) linked in series along the electrical current path during the SPS process. The equivalent circuit models in prior studies represented grain and grain boundary as "units-in-series", and each unit was simulated separately by a "resistor-capacitor-in-parallel" component set [31–35]; however, such "units-in-series" approach does not consider the possible passing current through ceramic compact during SPS, nor does it reflect the "units-in-parallel" nature of grains and grain boundaries. Our model treats every grain and its grain boundary as a whole "units-in-parallel" set, and then links grain/boundary sets along the current path as "units-in-series" circuit; furthermore, this model integrates the grain (Si_3N_4, represented by capacitor) and grain boundary (including TiC/TiN secondary phases and glassy phase, represented by resistor) into one unit set to reflect the obvious difference in their electrical characteristics. Evidently, the curve fitting results obtained using this model fit the actual better than those of other possible models.

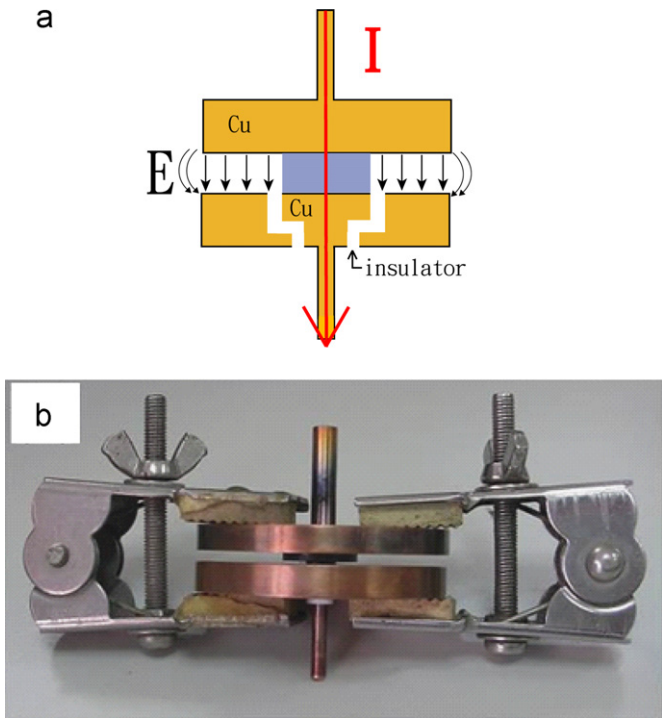

Fig. 1. A self-designed, parallel-plate sample fixture made of copper. The sample being tested was sandwiched between the top and bottom plates to ensure a uniform electric field distribution.

In Table 1, the total resistance (R_s) and capacitance (C_s) of the unit sets in series reveal the overall microstructural changes in the ceramic compacts. The total resistance in series was in the high giga-ohm range when the ceramic compact was porous. As the level of densification rose while the sintering temperature was increased from 1340 °C to 1600 °C (with dwell time = 0 min), R_s decreased to the lower giga-ohm region. Compared to the temperature increase, the dwell time had more influence on the reduction of electrical resistance. At the same sintering temperature of 1600 °C, the change in dwell time from 0 min to 3 min brought the electrical resistance of the ceramic compact to the mega-ohm region, a more than 1000-fold increase in the electrical conductivity. As the sintering temperature further rose to 1650 °C (dwell time = 3 min), the R_s increased from a few MΩ to ~400 MΩ. On the other hand, the total capacitance in series (C_s) increased monotonically as the sintering temperature and/or the dwell time increased as an indication of fewer grains linked in series. The smaller capacitance at lower temperatures was caused by the smaller Si_3N_4 grain size in the ceramic compact, and the resistance was influenced by both grain size and density (porosity) in the ceramic compact.

For the Si_3N_4/TiC and Si_3N_4/TiN nanocomposites, the TiC and TiN additives contributed the majority of the electrical conductivity to the sintered compact, and thus the resistance

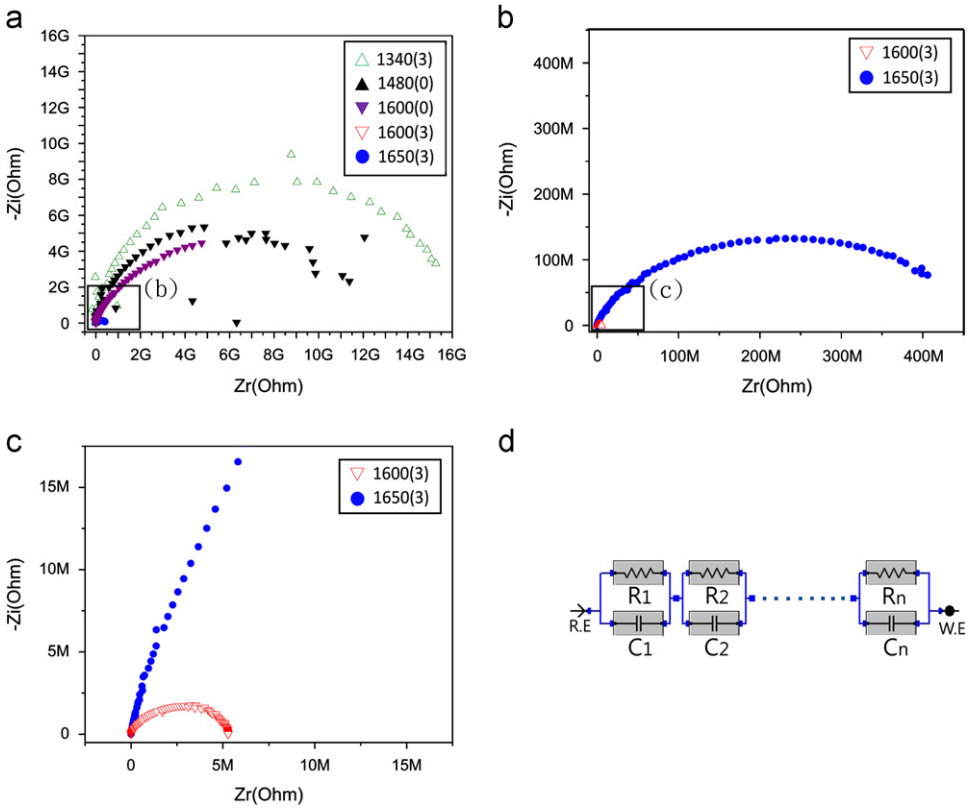

Fig. 2. Nyquist plots summarize the impedance responses of the Si_3N_4/10% TiC samples that underwent SPS at different temperatures (°C) and dwell times (number in the parentheses indicates minutes). (a) The overall spectrum in the giga-ohm range; (b) and (c) reveal the magnified regions of the Nyquist plots and show the impedance responses for $T=1600$ °C and 1650 °C; and (d) illustrates the equivalent circuit model used for the impedance analysis.

Table 1
Physical properties and fitted equivalent circuit model of Si_3N_4/10% TiC ceramic nanocomposites.

*Sinter par.	Properties			
	Density (g/cm^3)	Ave. grain size(nm)	R_s (total R in series)	C_s (total C in series)
1340 (0)	1.86	73	403 GΩ	18.62 pF
1480 (0)	2.21	76	26.7 GΩ	20.57 pF
1600 (0)	3.18	80	9.05 GΩ	37.77 pF
1600 (3)	3.34	102	5.2 MΩ	50.03 pF
1650 (3)	3.40	110	390 MΩ	52.17 pF

*The sintering parameters are given sintering temperature in *degreesCelsius* (dwell time in *minutes*).

in the equivalent circuit model is associated with the conductive secondary phases, while the capacitance of the ceramic compacts is associated with the Si_3N_4 phase, which dominates the capacitive characteristics as an insulator. During the spark plasma sintering, the presence of porosity affected R_s significantly, and the higher the density, the lower the R_s. The conductive additive was distributed among Si_3N_4 grains either as a secondary phase or grain boundary phase, and thus as the Si_3N_4 grains grew larger, the resistance of the conductive phase increased because of longer path and thinner boundary, explaining the increase in resistance at $T=1650$ °C.

3.2. Difference between TiC and TiN additives

Fig. 3 summarizes the typical microstructures of SPS Si_3N_4/TiC and Si_3N_4/TiN nanocomposites. The samples were sintered at 1650 °C for 3 min at a heating rate of 200 °C/min. The TiC and TiN phases are shown as the bright parts in the backscattered SEM images. For both the Si_3N_4/TiN and Si_3N_4/TiC samples, the amount of conductive nanopowders varied from 0 wt% to 20 wt%; the TiN was added up to 30 wt%, and the SEM image of the microstructures is also shown above. The existence

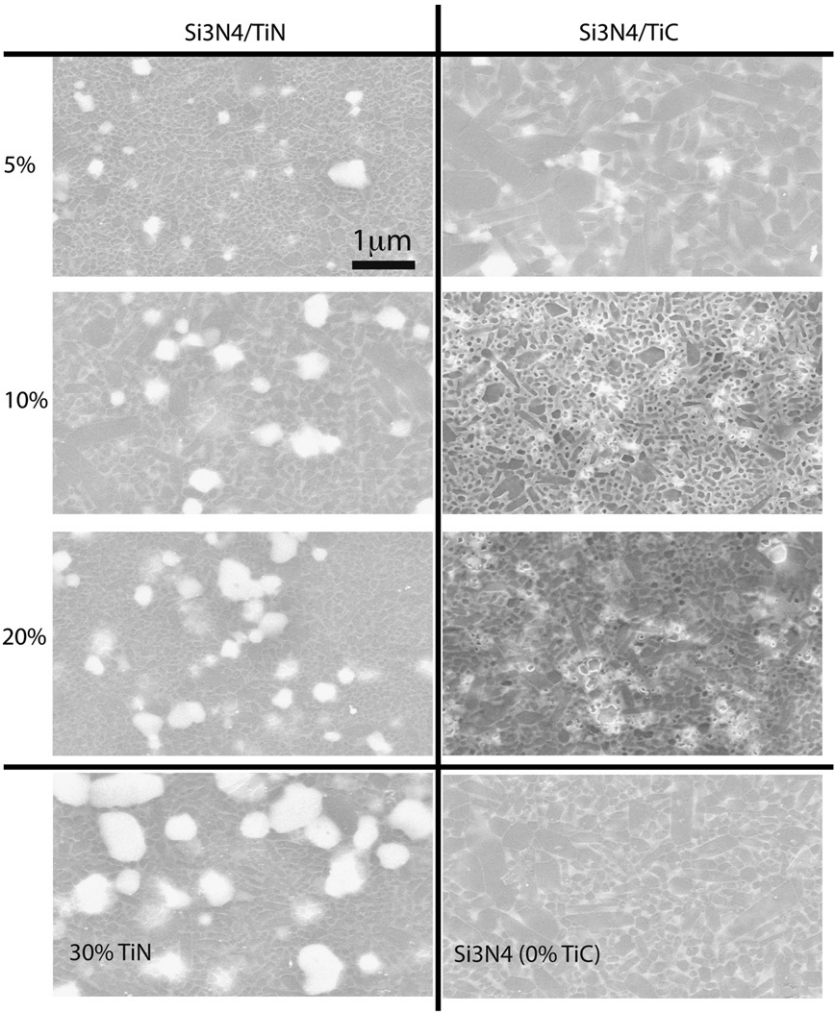

Fig. 3. Microstructures of the Si_3N_4/TiN and Si_3N_4/TiC samples with different weight percentages of conductive additives. The scale bar is 1 μm.

of the TiN and TiC phases prohibited grain boundary diffusion and the grain growth of Si_3N_4, with the exception of Si_3N_4/5TiC. The growth of elongated β-Si_3N_4 grains in Si_3N_4/5TiC is perhaps promoted by the pulse current during SPS. The addition of a conductive phase of TiC provided a pathway for leakage current under a pulse electric field, and this induced localized Joule heating which led to dynamic Ostwald ripening [26,36,37]. With the same weight percentage, the TiN secondary phase in the Si_3N_4/TiN samples formed large grains in the matrix, while the TiC phase in the Si_3N_4/TiC formed small grains in the Si_3N_4 matrix. For instance, the average grain size of TiN in Si_3N_4/10TiN was about 400 nm, whereas that of Si_3N_4/10TiC was about 100 nm. Both conductive phases were distributed discontinuously among the Si_3N_4 grains.

In addition to the grain size of secondary phase, the TiN and TiC additives in the nanocomposites exhibited dissimilar electrochemical behaviors. Figs. 4 and 5 summarize the Nyquist plots of the Si_3N_4/TiN and Si_3N_4/TiC nanocomposites with respect to the amount of conductive phases. As the electric resistivities of TiC, TiN, and Si_3N_4 are 1.8×10^{-4} to 2.5×10^{-4} Ω-cm, $\sim 2.5 \times 10^{-5}$ Ω-cm, and 10^{12}–10^{15} Ω-cm, respectively [38], the formation of the TiC and TiN conductive phases effectively introduced electric conductivity to the ceramic nanocomposites. The semicircular curves in the Nyquist plots indicates the capacitive characteristics of insulating Si_3N_4 grains, and the larger their span, the greater the insulating characteristic. Note that in prior studies on semiconducting ceramics [31,34,35], the impedance values decreased as grain size increased. The capacitive nature of Si_3N_4-based nanocomposites remained dominant in Si_3N_4/TiN with up to 30 wt% of conductive TiN nanopowders (Fig. 4), and in Si_3N_4/TiC with up to 10 wt% of TiC nanopowders (Fig. 5). In spite of the higher electric conductivity, the TiN additives did not effectively contribute to the electrical properties of the SPS nanocomposites, and the resistance of the Si_3N_4/30TiN ceramic was still in the giga-ohm region, while that of the Si_3N_4/10TiC ceramic was reduced to the mega-ohm region (Fig. 5(b)). In the inset of Fig. 5(b), the impedance response of Si_3N_4/20TiC was the same as that of an inductor, providing a clear indication of its conductive nature. The different impedance responses of the

Si_3N_4/TiN and Si_3N_4/TiC nanocomposites can be explained by the differences in their grain formation and conductive element distribution, as discussed earlier (Fig. 3). In particular, the large isolated TiN grains in the Si_3N_4 matrix did not form a conductive network at 30 wt%, while the impedance of the Si_3N_4/20TiC compact suggested the existence of a networked conductive phase, despite the lack of visual evidence under an electron microscope. It is believed that TiC diffused and distributed along Si_3N_4 grain boundaries in addition to forming TiC grains, constructing a conductive network (TiC grains and boundary phase having TiC), while TiN tended to form grains rather than diffusing into the grain boundaries.

3.3. Grain growth and impedance response

Another indication of TiC diffusion into grain boundaries is provided in the microstructure of Si_3N_4/5TiC. As discussed earlier, there was evidence of abnormal grain growth in the Si_3N_4/5TiC sample (Fig. 3), and the formation of exceptionally large Si_3N_4 grains is attributed to the Joule heating facilitated by the pulsed current passing through conductive TiC phases during spark plasma sintering. The impedance analysis shows that the 5 wt% of TiC additive in Si_3N_4 did not contribute sufficient conductivity to the ceramic compact to make it electrically appreciable (Fig. 5), and the microstructural characterization reveals isolated TiC grains; however, some trace amount of TiC could have distributed along Si_3N_4 grain boundaries and altered the local electric characteristics. As the result, the pulsed current might jump between discrete TiC grains and inter-grain glassy phase to connect the circuit. It is perhaps along such connecting pathways of electric current that the large elongated Si_3N_4 grains were grown. For highly conducting ceramics, such as Si_3N_4/20TiC, the networked conductive phase (via TiC grains and Si_3N_4 grain boundaries) could provide a uniform temperature distribution during sintering, thus preventing abnormal grain growth.

On the other hand, there was also normal grain growth in the Si_3N_4/20TiC samples caused by an increase in the sintering temperature. Fig. 6 shows the Nyquist plots of the Si_3N_4/20TiC samples with different average grain sizes. The sample with a grain size of 100 nm underwent SPS at 1600 °C with dwell time = 3 min, and the one with an average grain size of 300 nm underwent it at 1650 °C. From the Nyquist plots, it is clear that both nanocomposites had typical "resistor" behavior, and the resistance of the Si_3N_4/20TiC ceramic increased from 3 Ω to 31.5 Ω as the sintering temperature increased from 1600 °C to

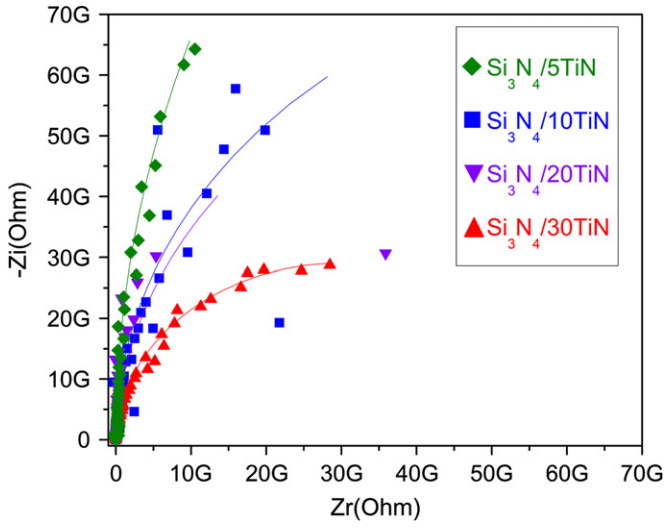

Fig. 4. Impedance spectra of Si_3N_4/TiN ceramic nanocomposites at various weight percentages of TiN.

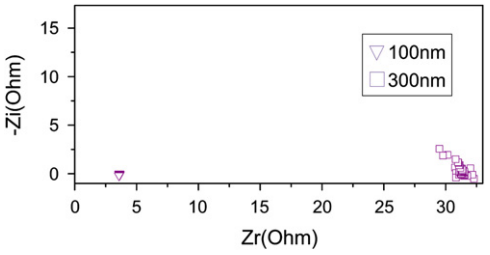

Fig. 6. Impedance responses of the Si_3N_4/20TiC samples with different average grain sizes.

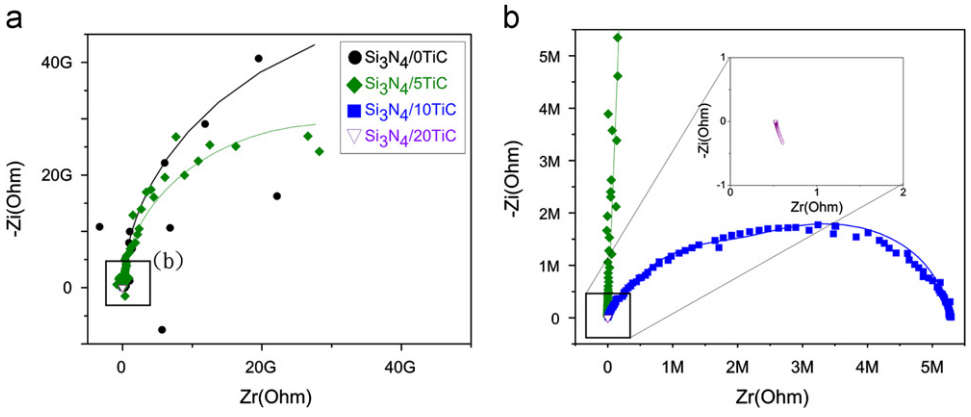

Fig. 5. Impedance spectra of Si_3N_4/TiC ceramic nanocomposites at various percentages of TiC. (a) Nyquist plot in the giga-ohm region and (b) Nyquist plot in the mega-ohm region to show more details. The inset revealed detail in the ohm region and show the impedance response of Si_3N_4/20TiC.

1650 °C. The increase in resistance with increasing average grain size coincides with the tunneling-percolation phenomenon proposed by Ambrosetti et al., which claimed that the conductivity of insulator-conductor nanocomposites was due to the tunneling current between two conductive phases [39]. Note in our cases, the tunneling-percolation effect can be assisted by the possible doping of TiC or Ti/C elements in the glassy grain boundaries. As the grain size increased, the characteristic tunneling length between the two conductive phases also increased, which led to a decrease in the tunneling current, and a rise in the resistance.

4. Conclusion

Spark plasma sintering is an effective method to fabricate Si_3N_4/TiC and Si_3N_4/TiN nanocomposites. The lower process temperature and shorter sintering time of SPS, and the pinning effect of the TiC and TiN grains, prevent the coalescence of Si_3N_4 grains thus make nano-sized microstructure possible. The addition of conductive second phases in Si_3N_4-based ceramics altered the electrical characteristics, as well as the microstructures in the SPS nanocomposites. The overall capacitance of Si_3N_4/TiC and Si_3N_4/TiN increased along with the grain size, while the resistance of the nanocomposites was influenced by porosity and grain size.

The equivalent circuit model for impedance analysis proposed in this work was able to link the microstructure evolution and impedance responses of ceramic, and to shed some light on the sintering mechanism of spark plasma sintering.

With an increasing weight percentage of the conductive second phase, the Si_3N_4-based nanocomposites transitioned from insulators to conductors. Based on the impedance model, the Si_3N_4/20% TiC seemed to have formed a conductive network in the microstructure, while the Si_3N_4/TiN nanocomposites still exhibited insulator behavior for up to 30 wt% addition of TiN. The microstructural and electrical differences in Si_3N_4/TiC and Si_3N_4/TiN can be explained by the different diffusive and distributive characteristics in TiC and TiN. TiN nanopowders in Si_3N_4-based ceramic compacts may have different sintering behaviors than TiC during SPS, and under same weight percentage, TiN formed larger grains than TiC did. The results of this work demonstrate that impedance measurement is a powerful tool for the study of the evolution of the microstructures of ceramic nanocomposites with conductive second phases. This approach also enables the further investigation of the densification mechanisms that occur during spark plasma sintering.

Acknowledgments

The authors gratefully acknowledge Prof. Chang-An Wang of Tsinghua University, China, for the help with SPS. This project was financially supported by the National Science Council of the ROC under Contract no. NSC 100-2221-E-006-121 and NSC 99-2923-E-006-002-MY3.

References

[1] B. Basu, J.-H. Lee, D.-Y. Kim, Development of nanocrystalline wear resistant Y-TZP ceramics, Journal of the American Ceramic Society 87 (9) (2004) 1771–1774.
[2] Y.H. Han, M. Nagata, N. Uekawa, K. Kakegawa, Eutectic Al_2O_3–$GdAlO_3$ composite consolidated by combined rapid quenching and spark plasma sintering technique, British Ceramic Transactions 103 (5) (2004) 219–222.
[3] Y.S. Kwon, D.V. Dudina, M.A. Korchagin, O.I. Lomovsky, Microstructure changes in TiB_2–Cu nanocomposite under sintering, Journal of Material Science 39 (16–17) (2004) 5325–5331.
[4] M. Nygren, Z. Shen, Novel assemblies via spark plasma sintering, Silicates Industriels 69 (7–8) (2004) 211–218.
[5] X.L. Su, P.L. Wang, W.W. Chen, Z.J. Shen, M. Nygren, Y.B. Cheng, D.S. Yan, Optical properties of SPS-ed Y- and (Dy,Y)-alpha-sialon ceramics, Journal of Material Science 39 (20) (2004) 6257–6262.
[6] M. Yue, J.X. Zhang, W.Q. Liu, G.P. Wang, Chemical stability and microstructure of Nd-Fe-B magnet prepared by spark plasma sintering, Journal of Magnetism and Magnetic Materials 271 (2–3) (2004) 364–368.
[7] L.J. Zhou, Z. Zhao, A. Zimmermann, F. Aldinger, M. Nygren, Preparation and properties of lead zirconate stannate titanate sintered by spark plasma sintering, Journal of the American Ceramic Society 87 (4) (2004) 606–611.
[8] D.M. Hulbert, A. Anders, D.V. Dudina, J. Andersson, D. Jiang, C. Unuvar, U. Anselmi-Tamburini, E.J. Lavernia, A.K. Mukherjee, The absence of plasma in ''spark plasma sintering'', Journal of Applied Physics 104 (3) (2008).
[9] T. Misawa, N. Shikatani, Y. Kawakami, T. Enjoji, Y. Ohtsu, H. Fujita, Observation of internal pulsed current flow through the ZnO specimen in the spark plasma sintering method, Journal of Materials Science 44 (6) (2009) 1641–1651.
[10] M. Nanko, T. Maruyama, H. Tomino, Neck growth on initial stage of pulse current pressure sintering for coarse atomized powder made of cast-iron, Journal of Japanese Institute of Metals 63 (7) (1999) 917–923.
[11] Z.A. Munir, D.V. Quach, M. Ohyanagi, Electric current activation of sintering—a review of the pulsed electric current sintering process, Journal of the American Ceramic Society 94 (1) (2011) 1–19.
[12] T. Misawa, N. Shikatani, Y. Kawakami, T. Enjoji, Y. Ohtsu, Influence of internal pulsed current on the sintering behavior of pulsed current sintering process, Material Science Forum 638–642 (2010) 2109–2114.
[13] M. Tokita, Development of advanced spark plasma sintering (sps) systems and its industrial applications, Ceramic Transactions 194 (2006).
[14] U. Anselmi-Tamburini, S. Gennari, J.E. Garay, Z.A. Munir, Fundamental investigations on the spark plasma sintering/synthesis process - II. Modeling of current and temperature distributions, Materials Science and Engineering A 394 (1–2) (2005) 139–148.
[15] W. Chen, U. Anselmi-Tamburini, J.E. Garay, J.R. Groza, Z.A. Munir, Fundamental investigations on the spark plasma sintering/synthesis process—I. Effect of dc pulsing on reactivity, Materials Science and Engineering A 394 (1–2) (2005) 132–138.
[16] K.Q. Dang, M. Kawahara, S. Takei, M. Nanko, Effects of pulsed current waveforms on sample temperature and sintering behavior in PECS of alumina, Journal of the Japan Society of Powder and Powder Metallurgy 56 (12) (2009) 780–787.
[17] M. Nanko, T. Oyaidu, T. Maruyama, Densification of Ni-20Cr alloy course-powder by pulse current pressure sintering, Journal of the Japanese Institute of Metals 66 (2) (2002) 87–93.
[18] G.Q. Xie, O. Ohashi, K. Chiba, N. Yamaguchi, M.H. Song, K. Furuya, T. Noda, Frequency effect on pulse electric current

sintering process of pure aluminum powder, Materials Science and Engineering A 359 (1–2) (2003) 384–390.
[19] K. Matsugi, H. Kuramoto, T. Hatayama, O. Yanagisawa, Temperature distribution at steady state under constant current discharge in spark sintering process of Ti and Al2O3 powders, Journal of Materials Processing Technology 146 (2) (2002) 34–37.
[20] D. Tiwari, B. Basu, K. Biswas, Simulation of thermal and electric field evolution during spark plasma sintering, Ceramics International 35 (2) (2008) 699–708.
[21] K. Vanmeensel, A. Laptev, O.V.d. Biest, J. Vleugels, Field assisted sintering of electro-conductive ZrO_2-based composites, Journal of the European Ceramic Society 27 (2–3) (2007) 979–985.
[22] W. Yucheng, F. Zhengyi, Study of temperature field in spark plasma sintering, Materials Science and Engineering B 90 (1–2) (2002) 34–37.
[23] A. Zavaliangos, J. Zhang, M. Krammer, J.R. Groza, Temperature evolution during field activated sintering, Materials Science and Engineering A 379 (1–2) (2004) 218–228.
[24] Q. Huang, D.T. Jiang, I.A. Ovid'ko, A. Mukherjee, High-current-induced damage on carbon nanotubes: the case during spark plasma sintering, Scripta Materialia 63 (12) (2010) 1181–1184.
[25] M. Belmonte, J. González-Julián, P. Miranzo, M.I. Osendi, Spark plasma sintering: a powerful tool to develop new silicon nitride-based materials, Journal of the European Ceramic Society 30 (14) (2010) 2937–2946.
[26] C.-H. Lee, H.-H. Lu, C.-A. Wang, P.K. Nayak, J.-L. Huang, Influence of conductive nano-TiC on microstructural evolution of Si3N4-based nanocomposites in spark plasma sintering, Journal of the American Ceramic Society 10 (1111/j) (2011) 1551–2916.
[27] D. Salamon, Z. Shen, P. Sajgalik, Rapid formation of alpha-sialon during spark plasma sintering: its origin and implications, Journal of the European Ceramic Society 27 (6) (2007) 2541–2547.
[28] Z. Shen, Z. Zhao, H. Peng, M. Nygren, Formation of tough interlocking microstructures in silicon nitride ceramics by dynamic ripening, Nature 417 (2002) 266–269.
[29] M. Suganuma, Y. Kitagawa, S. Wada, N. Murayama, Pulsed electric current sintering of silicon nitride, Journal of the American Ceramic Society 86 (3) (2003) 387–394.
[30] H.-L. Chiu, J.-L. Huang, Microstructure and fracture behavior of hot-pressed TiC/Si_3N_4 composite, Ceramics International 20 (1) (1994) 49–55.
[31] T.B. Adams, D.C. Sinclair, A.R. West, Characterization of grain boundary impedances in fine- and coarse-grained $CaCu_3Ti_4O_{12}$ ceramics, Physical Review B 73 (2006).
[32] P. Dhak, D. Dhak, M. Das, K. Pramanik, P. Pramanik, Impedance spectroscopy study of $LaMnO_3$ modified $BaTiO_3$ ceramics, Materials Science and Engineering B: Advanced 164 (3) (2009) 165–171.
[33] M.J. Jørgensen, M. Mogensen, Impedance of solid oxide fuel cell LSM/YSZ composite cathodes, Journal of the Electrochemical Society 148 (2001) 433.
[34] S.J. Luo, G. Fu, H. Chen, Z.Y. Liu, Q.S. Hong, Gas-sensing properties and complex impedance analysis of Ce-added WO_3 nanoparticles to VOC gases, Solid State Electronics 51 (6) (2007) 913–919.
[35] M. Miyayama, H. Yanagida, Dependence of grain-boundary resistivity on grain-boundary density in yttria-stabilized zirconia, Communications of the American Ceramic Society (1984) 194.
[36] J. Liu, Z.J. Shen, M. Nygren, Y.M. Kan, P.L. Wang, SPS processing of bismuth-layer structured ferroelectric ceramics yielding highly textured microstructures, Journal of the European Ceramic Society 26 (15) (2006) 3233–3239.
[37] Z.J. Shen, H. Peng, J. Liu, M. Nygren, Conversion from nano- to micron-sized structures: experimental observations, Journal of the European Ceramic Society 24 (12) (2004) 3447–3452.
[38] NIST, Standard Reference Database: Materials, in, NIST, 2010. 〈http://www.nist.gov/srd/materials.cfm〉.
[39] G. Ambrosetti, C. Grimaldi, I. Balberg, T. Maeder, A. Danani, P. Ryser, Solution of the tunneling-percolation problem in the nanocomposite regime, Physical Review B 81 (15) (2010) 155434.